CrossMark

X-Ray Intraday Variability of the TeV Blazar Markarian 421 with XMM-Newton

A Priyana Noel[1] , Haritma Gaur[2] , Alok C. Gupta[2] , Alicja Wierzcholska[3] , Michał Ostrowski[1] , Vinit Dhiman[2] , and
Gopal Bhatta[3]

[1] Astronomical Observatory of the Jagiellonian University, Kraków, Poland; anoel@oa.uj.edu.pl
[2] Aryabhatta Research Institute of Observational Sciences (ARIES), Manora Peak, Nainital − 263 001, India
[3] Institute of Nuclear Physics, Polish Academy of Sciences, PL-31342 Krakow, Poland

Abstract

Highly variable Markarian 421 is a bright high–synchrotron energy peaked blazar showing a wide featureless nonthermal spectrum, making it a good candidate for our study of intraday flux and spectral variations over time. We analyze its X-ray observations over 17 yr, taken with the EPIC-pn instrument, to probe into the intraday variability properties, focusing on the photon energy band of 0.3–10.0 keV, and its soft (0.3–2.0 keV) and hard (2.0–10.0 keV) subbands. To examine the flux variability, fractional variability amplitudes and minimum variability timescales have been calculated. We also probed into the spectral variability by studying the hardness ratio for each observation, the correlation between the two energy bands, using the discrete correlation function, and inspecting the normalized light curves. The parameters obtained from these methods were studied for any correlations or nonrandom trends. From this work, we speculate on the constraints on the possible particle acceleration and emission processes in the jet, for a better understanding of the processes involving turbulent behavior, except for shocks. A positive discrete correlation function between the two subbands indicates the role of the same electron population in the emission of photons in the two bands. A correlation between the parameter of flux variability and the parameters of spectral variation and lags in the subenergy bands provides the constraints to be considered for any modeling of emission processes.

1. Introduction

Blazars exhibit flux and spectral variability at all wavelengths of the observable electromagnetic (EM) spectrum, strong polarization ($>3\%$) from the radio to optical bands, and are accompanied by core-dominated radio structures. Based on the unified model for radio-loud (RL) active galactic nuclei (AGNs), blazars emit jets in the direction toward the Earth (Urry & Padovani 1995). Blazars are a subclass of RL AGNs, which can be further split into BL Lacertae (BL Lac) objects and flat-spectrum radio quasars (FSRQs). BL Lac objects show largely featureless composite optical to ultraviolet (UV) spectra and have predominant nonthermal EM spectra, while FSRQs show prominent emission lines.

Multiwavelength (MW) spectral energy distributions (SEDs) of blazars are characterized by a broad double-peaked structure in the logarithmic plot of νf_ν versus ν (Ghisellini et al. 1997). The low-energy SED peak situated from infrared to X-ray energies is due to the synchrotron radiation of relativistic nonthermal electrons in the jet. The high-energy peak ranges from MeV to TeV γ-ray energies and can be explained by leptonic or hadronic emission models. According to the leptonic model, the high-energy emission is due to inverse Compton (IC) upscattering of the synchrotron (also called the synchrotron self-Compton or SSC model or ambient photons by the highly relativistic electrons in the jet (e.g., Kirk et al.

1998; Gaur et al. 2010). The hadronic emission models invoke either proton–photon cascade processes or synchrotron emission of extremely highly energetic protons (e.g., Mücke et al. 2003).

Based on the location of the low-energy peak in the SED, blazars are further classified into low-energy peaked blazars (LBLs) and high-energy peaked blazars (HBLs, also called HSP; Padovani & Giommi 1995). In LBLs, the first peak of the SED is visible in the near-infrared/optical frequency range, and in HBLs, it is visible in the UV/X-ray photon energies. The second peak lies in GeV γ-ray energies in LBLs and in TeV γ-ray energies in HBLs.

Blazars display flux and spectral variability in the EM spectrum over a wide range of timescales, so simultaneous MW observations are preferred when studying them. Flux variations with timescales from a few minutes to less than a day are commonly known as blazar microvariability (Miller et al. 1989), intraday variability (IDV; as in Wagner & Witzel 1995), or intranight variability (for example, Goyal et al. 2009). When a variability timescale from several days to a few months is studied, it is referred to as short-term variability, while flux variations from months to years are described as long-term variability (as in Gupta et al. 2004).

Another characteristic observed in blazars is the formation of loops in the hardness ratio–intensity (HR–I) diagrams, due to spectral hysteresis. As suggested Kirk et al. (1998), a lag in the photons occurs between different energy bands, because of difference in the acceleration and cooling times of the electrons. Sambruna (2000) pointed out that a soft-emission lag leads to a clockwise loop, while a hard-photon lag results in an anticlockwise loop in the HR–I diagram.

In the present paper, we study the detailed X-ray IDV properties of the blazar Markarian 421, using a long series of XMM-Newton satellite data. The blazar is also commonly known as Mkn 421 and Mrk 421 ($\alpha_{2000.0} = 11^h04^m27^s2$ and $\delta_{2000.0} = +38°12'32''$). Mrk 421 was first noted as a stellar-like object with a blue excess coinciding with a point-like bright nucleus of the elliptical galaxy. It was classified as a BL Lac object due to its featureless optical spectrum, compact radio emission, and strongly polarized and variable fluxes in the optical and radio bands (Ulrich et al. 1975). It is one of the nearest blazars, at redshift $z = 0.0308$ (Ulrich et al. 1975), equivalent to the distance of 134 Mpc.[4] By using the spectra of its host galaxy, the central super massive black hole (SMBH) mass was evaluated to be $(2-9) \times 10^8\,M_\odot$ (e.g., Falomo et al. 2002; Wu et al. 2002; Barth et al. 2003). The synchrotron peak in the SED of Mrk 421 was found in X-ray energies higher than 0.1 keV, and thus the object was classified as an HBL/HSP blazar. It was the first extragalactic object from which TeV γ-ray emission was detected (Punch et al. 1992). GeV γ-ray emission was detected from Mrk 421 by the Energetic Gamma Ray Experiment Telescope on board the Compton Gamma Ray Observatory satellite (Lin et al. 1992; Michelson et al. 1992). By using observations of the source from various ground-based Cherenkov γ-ray telescopes, it has been repeatedly observed as a TeV γ-ray emitting source (Schubnell et al. 1993; Acciari et al. 2011; Abeysekara et al. 2017).

Mrk 421, as well as other TeV emitting blazars, have been comprehensively observed in X-ray and γ-ray energies to study their flux and spectral variability properties (e.g., Maraschi et al. 1999; Fossati et al. 2000b, 2000c; Malizia et al. 2000; Brinkmann et al. 2001, 2003, 2005; Sembay et al. 2002; Ravasio et al. 2004; Tramacere et al. 2007, 2009; Isobe et al. 2010; Pian et al. 2014; Kataoka & Stawarz 2016; Pandey et al. 2017; Aggrawal et al. 2018; Zhang et al. 2019, and references therein). This bright source is among the most extensively studied blazars in the observable EM spectrum, due to its strong flux and spectral variabilities and emission detected up to TeV energies. The object has been a goal of several simultaneous MW observational campaigns over extended periods of time (Błażejowski et al. 2005; Fossati et al. 2008; Lichti et al. 2008; Donnarumma et al. 2009; Horan et al. 2009; Acciari et al. 2011; Alekssić et al. 2015a, 2015b; Acciari et al. 2020). In X-rays, Mrk 421 shows very complex flux and spectral variability (see Gupta 2020 for a review). MW observations of this source are used for fitting different emission models, involving, e.g., a combination of SSC and IC processes, and occasionally leptohadronic models are applied (see Gupta 2020 for a review).

It is known that many blazars are characterized by flux variations on IDV timescales in different EM bands (e.g., Miller et al. 1989; Gaur et al. 2010; Kalita et al. 2015; Gupta et al. 2016; Aggrawal et al. 2018; Gupta 2018; Zhang et al. 2019, and references therein). The most puzzling and not yet well understood flux variations in blazars are those observed on IDV timescales that are most probably directly related to the activity in the close vicinity of the central SMBH of the blazar. In such a case, the flux variability can be applied to constrain the size and relativistic kinematics of the emitting region, and the level of variability may strongly depend on the SMBH mass (Markowitz & Edelson 2004).

To work on the intriguing issue of blazar flux variability on IDV timescales, some of us involved in this collaborative work have initiated a pilot project in X-ray energies based on the data of blazars taken from the public archives of various X-ray missions (e.g., XMM-Newton, NuStar, Chandra, and Suzaku), as reported in a series of papers (Lachowicz et al. 2009; Gaur et al. 2010; Bhagwan et al. 2014, 2016; Kalita et al. 2015; Gupta et al. 2016; Pandey et al. 2017, 2018; Aggrawal et al. 2018; Zhang et al. 2019, 2021; Dhiman et al. 2021).

Significant efforts have been devoted by several researchers to study XMM-Newton observations of Mrk 421, applying various analysis techniques to the same observational data that we reanalyze in the present study. Brinkmann et al. (2001) published the results of the first observation of Mrk 421 taken on 2000 May 25, from the XMM-Newton satellite. They reported that the source is more variable at higher energies than at lower-energy bands, where the low-energy bands were taken as being below 1 keV and the high-energy bands were taken as being above 3 keV. Peretz & Behar (2018) conducted a classification of AGNs on the basis of X-ray variability, in which they reported that, for RL AGNs and blazars, the variability at higher energies dominates over the lower-energy range. Ravasio et al. (2004) analyzed the flaring in three observations of Mrk 421. They discussed the nonreliability of reporting a spectral lag using a discrete correlation function (DCF; in our work, we also note that DCF is not a robust way of studying such lags in cases of light curves (LCs) involving regular time trends). The HR–I diagram of the flaring part of the LC for these three observations formed a loop, indicating spectral hysteresis. Yan et al. (2018) analyzed all the observations of Mrk 421 taken from the XMM-Newton satellite. The authors fitted the flares of the LCs, obtaining a power-law distribution that is a signature of a self-organized criticality model, which can explain the flaring with involved magnetic reconnection processes.

Our new analysis of the XMM-Newton extended series of Mrk 421 X-ray observations involves a multiparameter study of the considered individual observational runs, before comparing all the observations to reveal the general trends (or the lack of such trends) essential for the understanding the blazar X-ray emission-generating processes. We utilize public archival data of 25 pointed observations of Mrk 421 with the EPIC-pn instrument on board XMM-Newton, carried out over a period of 17 yr (2000–2017), to analyze the flux and spectral variations on IDV timescales and to study the X-ray emission that is tentatively expected to be generated in the jet close to the central BH of the blazar. The paper is arranged as follows. In Section 2, we discuss the EPIC-pn public archival data and its analysis. Section 3 provides a brief description of the analysis techniques used in this study. In Section 4, the results of the data analysis are presented. A discussion and conclusions then follow in Section 5.

2. XMM-Newton Observations and Data Reduction

There are 55 pointed observations of Mrk 421 from 2000 May 25 to 2017 May 4, taken with EPIC-pn on board the XMM-Newton satellite. The best 25 observations selected for our analysis, with a minimum duration of 10 ks, are listed in Table 1. Below, we provide information about the XMM-Newton satellite, the EPIC-pn data, and the data reduction and analysis performed.

---

[4] Throughout this paper, we use $H_0 = 71$ km s^{-1} Mpc^{-1}, $\Omega_m = 0.27$, and $\Omega_\lambda = 0.73$.

Table 1
The Analyzed Mrk 421 Observations from the EPIC-pn Instrument on Board XMM-Newton

Obs. ID	Date of Obs. (yyyy–mm–dd)	Window Mode	Obs. Duration (ks)	Pileup	Filter
0099280101	2000–05–25	Small	66.4	yes	Thick
0099280201	2000–11–01	Small	40.1	yes	Thick
0099280301	2000–11–13	Small	49.8	yes	Thick
0136540101	2001–05–08	Small	39.0	yes	Thin 1
0136541001	2002–12–01	Timing	71.1	no	Medium
0158970101	2003–06–01	Small	47.5	yes	Thin 1
0150498701	2003–11–14	Timing	49.3	no	Thin 1
0162960101	2003–12–10	Small	50.7	yes	Medium
0158971201	2004–05–06	Timing	66.1	no	Medium
0153951201	2005–11–07	Timing	10.0	no	Thin 1
0158971301	2005–11–09	Timing	60.0	no	Thick
0302180101	2006–04–29	Timing	41.9	no	Thin 1
0411080301	2006–05–28	Small	69.2	yes	Medium
0411080701	2006–12–05	Timing	18.9	no	Medium
0510610101	2007–05–08	Timing	27.6	no	Medium
0510610201	2007–05–08	Timing	22.7	no	Medium
0502030101	2008–05–07	Timing	43.2	no	Thin 1
0670920301	2014–04–29	Timing	16.2	no	Thin 1
0670920401	2014–05–01	Timing	18.0	no	Thin 1
0670920501	2014–05–03	Timing	18.0	no	Thin 1
0658801301	2015–06–05	Small	29.0	yes	Thick
0658801801	2015–11–08	Small	33.6	yes	Thick
0658802301	2016–05–06	Small	29.4	yes	Thick
0791780101	2016–11–03	Small	17.5	no	Thick
0791780601	2017–05–04	Small	12.5	yes	Thick

2.1. XMM-Newton Satellite

XMM-Newton is an X-ray astronomy mission of the European Space Agency, launched in 1999. The satellite has a 48 hr period of orbit revolution, with a perigee of 7000 km and an apogee of 114,000 km. It has six coaligned instruments on board—three European Photon Imaging Cameras (EPIC), two Reflection Grating Spectrometers (RGS), and one Optical Monitor telescope.

EPIC is an X-ray instrument on board XMM-Newton with one CCD of the pn type and two other CCDs of the metal oxide semiconductor (MOS) type, each with approximately 1500 cm^2 of geometric effective area and a large field of view of 30′ diameter. The photon energy range of the operation of the EPIC instruments is 0.15−15 keV. The EPIC-pn telescope has a higher time resolution than the EPIC MOS telescope. The time resolutions of the seven CCDs of the pn telescope are 30 μs in the timing and burst modes. The X-ray MOS CCDs are placed behind the telescope that contains the grating of the RGS. The grating redirects half of the incident flux to the RGS detectors, while 40% of the incident flux is channeled toward the MOS cameras. This makes the pn instrument better for flux variability studies than the MOS instrument.

2.2. Data Selection

The data comprising the observations from the pn camera were downloaded from the XMM-Newton Science Archive.[5] In our work, in order to study the IDV properties of Mrk 421, we require high-quality observations, with each individual run being longer than 10 ks (∼3 hr), and only those observations

have been selected for the analysis. The data taken from the pn instrument were selected because of the higher sensitivity and lower photon pileup effects of the EPIC-pn instrument as compared to the EPIC MOS instrument. Along with the explanation given in Section 2.1, this is the reason why only data from the pn instrument have been used. For the same reasons, other authors, like Gaur et al. (2010), Bhagwan et al. (2014), Mohorian et al. (2021), and Pavana Gowtami et al. (2022), have also only used pn data.

There are a total 55 archived observations from the pn instrument from the beginning of the satellite's operation until 2017 June. Out these, 30 observations were excluded for a number of quality- and time-related reasons—spurious detections in 20 observations, no science products in two observations, no target visible in five observations, and seven observations having an observation time of less than 10 ks. Mrk 421 has been observed as having a minimum variability timescale of 5.5 ks in a previous study by Aggrawal et al. (2018), and 1.1 ks in a study by Chatterjee et al. (2021), using Chandra and Astrosat data. Shorter observations than the variability timescale may not show variability properties, thus observations greater then 10 ks were chosen, to be able to study the variability property of the source over scales of minutes and a few hours. Thus, after considering these conditions, there were 25 observations left for accomplishing our goal of conducting IDV studies. These 25 observations, as shown in Table 1, were taken in small-window mode or timing mode. The time resolution for the small-window mode of the pn instrument is 5.7 ms, while for the timing mode it is 0.03 ms. Thus, these observations are useful for studying the variability over a scale of seconds.

---

[5] http://nxsa.esac.esa.int/nxsa-web/#search

2.3. Data Analysis

The data analysis was performed using Science Analysis Software.[6] The instrument's science data, housekeeping, and auxiliary files that were needed to perform the analysis are packed together as the Observation Data Files (ODFs) in the XMM-Newton data archive, where the Current Calibration Files are also available for data calibration. To obtain an updated list of the calibration files, a task *cifbuild* was used, with the task *odfingest*, to create a summary file of all the components in the ODF set. The task *epchain* consists of a set of tasks performed over pn data to produce an event list.

Mrk 421 is a bright blazar generating photon pileup effects. Pileup effects are produced when two or more photons fall on the same pixel or neighboring pixel, and the detector counts it as one photon event, with the sum of the energies of the falling photons. The model distribution of single-photon events is compared to double-photon events, and if the two do not overlap, then this signifies the presence of pileup. If both distributions are comparable, then it means that there are no significant pileup effects. To correct for pileup, the circular core influenced by the effect of the PSF was excised and an annular region without pileup was selected for the analysis of this point source. The task *epatplot* was used to check and correct it.[7]

In the analysis, we use the data from the limited energy range, from 0.3 keV to 10.0 keV, as there is known detector noise below 0.3 keV and the measurements above 10.0 keV are subject to a high-proton background caused by solar activity (Gaur et al. 2010; Bulbul et al. 2020). We monitored such effects by checking the derived LCs in this energy range. For uniformity, all the observations have been binned to 100 s, which helps to study variability on a timescale of minutes.

3. Procedures Applied in the Analysis

In this section, we present the data analysis techniques and methods used in the paper to study the LCs of the individual observations. All the LCs were binned to 400 s for the data to be consistent throughout.

3.1. Excess Variance

One of the parameters that we use to assess the Mrk 421 variability is excess variance (Vaughan et al. 2003). This is derived from the difference between the total variance of the fluxes measured along the LCs and the total variance generated by the measurement errors. For N being a number of the measured flux values along the LC, x_i, and having corresponding uncertainties $\sigma_{\text{err},i}$ arising from the measurement errors, the excess variance, σ_{XS}^2, is derived as

$$\sigma_{XS}^2 = S^2 - \overline{\sigma_{\text{err}}^2}, \tag{1}$$

where S^2 is the variance along the given observational sample LC, given by

$$S^2 = \frac{1}{N-1}\sum_{i=1}^{N}(x_i - \bar{x})^2, \tag{2}$$

where $\bar{x}$ is the arithmetic mean of x_i, and the mean square error is

$$\overline{\sigma_{\text{err}}^2} = \frac{1}{N}\sum_{i=1}^{N}\sigma_{\text{err},i}^2. \tag{3}$$

The fractional rms variability amplitude, denoted by F_{var}, is defined as the square root of the normalized excess variance,

$$F_{\text{var}} = \sqrt{\frac{S^2 - \overline{\sigma_{\text{err}}^2}}{\bar{x}^2}}, \tag{4}$$

with an uncertainty of F_{var},

$$\text{err}(F_{\text{var}}) = \sqrt{\left(\sqrt{\frac{1}{2N}}\frac{\overline{\sigma_{\text{err}}^2}}{\bar{x}^2 F_{\text{var}}}\right)^2 + \left(\sqrt{\frac{\overline{\sigma_{\text{err}}^2}}{N}}\frac{1}{\bar{x}}\right)^2}. \tag{5}$$

This procedure has been used to quantify the flux variability of the source in the total-energy band (0.3–10.0 keV) studied, as well as in its hard (2.0–10.0 keV) and soft (0.3–2.0 keV) subbands.

3.2. Minimum Timescale of Flux Variability

The minimum two-point flux variability timescale can be calculated as given by Burbidge et al. (1974):

$$\tau_{\text{var}} = \text{Minimum}\left\{\left|\frac{\Delta t}{\Delta \ln(x)}\right|\right\}, \tag{6}$$

where we select the minimum value from the series of all pairs $(i, i+1)$ of the two successive data points, along the LC, $\Delta t_{i,i+1} = t_{i+1} - t_i$, and the respective $\Delta \ln x = (x_{i+1} - x_i)/x_i$. To account for the effects of the uncertainties in the flux measurements in the calculation of the variability timescales, in these formal derivations we impose the condition that $|x_i - x_{i+1}| > \sigma_{x_i} + \sigma_{x_{i+1}}$, and treat all the analyzed data uniformly, irrespective of the possible gaps in the observations (Bhatta et al. 2018; Zhang et al. 2019). The uncertainties in τ_{var} are calculated using the respective count rates, x_j and x_{j+1}, leading to the shortest variability timescale, with Δx_j and Δx_{j+1} being their corresponding uncertainties:

$$\Delta\tau_{\text{var}} \simeq \sqrt{\frac{x_j^2 \Delta x_{j+1}^2 + x_{j+1}^2 \Delta x_j^2}{x_j^2 x_{j+1}^2 (\ln[x_j/x_{j+1}])^4}}\,\Delta t_{j,j+1}. \tag{7}$$

The above weighted variability timescales were calculated using the LCs for the total-energy range from 0.3 to 10.0 keV.

3.3. Hardness Ratio

The HR is an efficient parameter for studying the spectral variations of the source along its LC, having an advantage over full spectral modeling because of the possibility of studying short time bins of the LC with low count statistics in each bin. We define the HR in each time bin analyzed as a simple ratio of the photon counts in the selected hard- and soft-energy bands (Park et al. 2006). The physical meaning of the HR values depends on a number of factors related to the emission parameters of the source, which are usually poorly known. One may expect the observed HR changes to describe the physical changes in the emitting source if the soft and hard ranges under study are related to different spectral components in the full spectrum.

Following other authors (e.g., Peretz & Behar 2018), we decided to select an energy scale of 2 keV for splitting the observational energy range studied into soft (S; 0.3–2.0 keV) and hard (H; 2.0–10.0 keV) subranges, to keep the hard-energy range limited to relatively high energies, while also still preserving a reasonable number of high-energy photons and limiting HR statistical fluctuations. To derive the HR of each time bin along the LC, we use photon counts, H and S, in the respective energy subranges:

$$HR = \frac{H}{S}, \tag{8}$$

where we use the *lcurve* task of the XRONOS program from HEASARC.

3.4. Discrete Correlation Function

When the LCs are unevenly binned, the classical correlation function (CCF) technique, which is based on the interpolation between the data points, is not precise in deriving correlations between the compared LCs. In this case, a DCF technique (Edelson & Krolik 1988) can be used, similar to the CCF, but with the additional advantages of not having to deal with binned data sampling and interpolating in time. DCF is employed here to check the correlation between the flux variabilities in the hard- and soft-energy bands. In the applied procedure, we first compute the unbinned correlation, called the unbinned discrete correlation function (UDCF), for the data in the aforementioned energy bands (Pandey et al. 2017) as

$$UDCF_{jk} = \frac{(S_j - \bar{S})(H_k - \bar{H})}{\sqrt{\sigma_S^2 \sigma_H^2}}, \tag{9}$$

where S_j and H_k are the "jth" and "kth" data points in the energy bands S and H, $\bar{S}$ and $\bar{H}$ are their mean values, and σ_S^2 and σ_H^2 are their variances, respectively. Each pair (S_j, H_k) is associated with a pairwise time lag $\Delta t_{jk} = t_j - t_k$. The time binning of the UDCF is done with a value depending on the bin times of the LCs in both energy bands. To calculate the DCF for each time lag τ, we use the average result of the UDCF. Averaging is performed over all $UDCF_{jk}$, satisfying the condition $\tau - (\Delta\tau/2) \leqslant \Delta t_{jk} \leqslant \tau + (\Delta\tau/2)$:

$$DCF(\tau) = \frac{1}{N}\sum UDCF_{jk}, \tag{10}$$

where the summation of the values of the UDCF calculated over all the permutations of j and k is taken. One should note that, in general, the DCF between two LCs is not normalized to 1.

To find the respective time lag, μ, between the energy bands studied, we fit a Gaussian function to the DCF plot near its maxima (Zhang et al. 2019):

$$DCF(\tau) = Ae^{-(\tau-\mu)^2/2\sigma^2}, \tag{11}$$

where A is the maximum value of the DCF, μ is the time lag at which the DCF peaks, and σ is the fitted width of the Gaussian function. For each DCF, we select a limited range of τ, where the maximum structure allows for a reasonable Gaussian fit.

3.5. Normalized Hard and Soft Light Curves

The photon counts in the hard and soft bands were normalized by dividing the flux values (photon counts) in each time bin by the average photon count in the respective band (Urry et al. 1997). The normalized LCs are plotted simultaneously against each other, to understand the trends of hard versus soft X-ray photons over time, and to independently evaluate the integral information provided by the DCF, in particular the derived time lag of the photons in the two energy bands. Visual comparison of the normalized LCs reveals real lags and nonuniformities between the individual LC fluctuations.

3.6. The Source Variability Duty Cycle

Estimation of the source variability duty cycle (DC) is commonly used for estimation of the time fraction over which the source exhibits time variability. We estimated the DC for Mrk 421 using the standard approach of Romero et al. (1999) with the definition that he gives in his work, which has since been used by many groups of authors (e.g., Agarwal et al. 2016; Aggrawal et al. 2018, and references therein):

$$DC = 100\% \cdot \frac{\sum_{i=1}^{n} N_i \Delta t_i}{\sum_{i=1}^{n} \Delta t_i}, \tag{12}$$

where we use the time duration, Δt_i, of the *i*th observation run (Observation ID), and N_i takes the value 0 for no IDV detection and 1 whenever IDV is detected, with the condition $F_{var} > 3 \times (F_{var})_{err}$ for the detection of IDV variability.

4. Results

The 25 selected pointed X-ray observations of Mrk 421 from the EPIC-pn instrument on board XMM-Newton provide us with the opportunity to carry out analyses of the flux variability and spectral variability, and cross-correlated studies of the soft and hard X-ray bands of the blazar, on IDV timescales over 17 yr of observations. For the individual Observational IDs, the observation times in our sample varied from 10 to 71.1 ks. The detailed observation log is given in Table 1, and a set of analysis results is given in Table 2. Here, we only present the plots obtained for observation 0099280101, with the plots for all the other observations being provided in the online figure set.

4.1. Descriptions of Individual Observations

To start, let us analyze all the individual Observation IDs by studying a set of plots including the LC in the total-energy band, the LCs in the soft and hard bands, the HR–I diagram, the plot of HR versus time, the normalized LCs, and the plot of the derived DCF. Some extra plots are added for cases where we compare our results with earlier works.

4.1.1. Obs. ID 0099280101

The 66.4 ks observation of Mrk 421 (see Figure 1) displays high values of fractional variability, of 10.16%, 16.49%, and 9.25%, in the total-, hard-, and soft-energy bands, respectively. There are two visible flares in this observation, one from the beginning of the observation and the other starting at ∼24 ks. The variable HR of the emission shows a clear harder-when-brighter behavior in the HR–I plot. No systematic trends are

Table 2
X-Ray Variability Parameters of Mrk 421

| Number | Obs ID | $\bar{x}$ | F_{var} (%) | | | τ_{var} (ks) | A | μ (ks) | σ (ks) |
			Soft (0.3–2.0 keV)	Hard (2.0–10.0 keV)	Total (0.3–10.0 keV)				
1	0099280101	317	9.25 ± 0.07	16.49 ± 0.19	10.16 ± 0.07	3.78 ± 0.41	0.99	0.03	6.5 ± 0.0
2	0099280201	130	9.14 ± 0.08	10.44 ± 0.28	9.17 ± 0.08	4.81 ± 0.65	0.90	2.44	9.8 ± 0.4
3	0099280301	496	3.03 ± 0.05	12.86 ± 0.13	4.12 ± 0.04	4.50 ± 0.54	0.77	−0.19	2.3 ± 0.1
4	0136540101	438	5.09 ± 0.06	12.45 ± 0.19	5.76 ± 0.06	3.41 ± 0.33	0.88	−0.21	1.6 ± 0.2
5	0136541001	291	3.41 ± 0.03	6.61 ± 0.09	3.62 ± 0.02	4.19 ± 0.31	0.83	−1.11	4.7 ± 0.7
6	0158970101	329	6.27 ± 0.07	8.78 ± 0.28	6.35 ± 0.07	2.51 ± 0.24	0.67	2.56	7.9 ± 0.7
7	0150498701	694	7.61 ± 0.05	17.61 ± 0.17	8.29 ± 0.05	2.96 ± 0.16	0.77	1.71	7.4 ± 0.6
8	0162960101	362	2.79 ± 0.08	4.62 ± 0.26	2.91 ± 0.08	2.61 ± 0.27	0.71	0.04	4.5 ± 1.1
9	0158971201	850	9.51 ± 0.03	22.85 ± 0.06	11.61 ± 0.02	5.96 ± 0.52	0.94	−0.38	2.2 ± 0.2
10	0153951201	678	4.30 ± 0.19	6.41 ± 0.59	4.50 ± 0.18	7.02 ± 0.59	0.89	0.23	3.1 ± 0.2
11	0158971301	748	11.11 ± 0.04	15.11 ± 0.11	11.53 ± 0.04	4.53 ± 0.33	0.96	1.31	19.6 ± 2.2
12	0302180101	537	3.87 ± 0.02	8.93 ± 0.07	4.43 ± 0.02	10.59 ± 0.79	0.87	−0.19	3.9 ± 1.2
13	0411080301	822	3.69 ± 0.05	8.19 ± 0.14	4.33 ± 0.05	5.46 ± 0.53	0.88	0.31	5.3 ± 0.3
14	0411080701	302	1.13 ± 0.05	2.59 ± 0.22	1.18 ± 0.06	5.78 ± 0.45	0.62	−0.94	5.9 ± 2.8
15	0510610101	265	1.21 ± 0.04	3.36 ± 0.22	1.32 ± 0.04	4.69 ± 0.34	0.76	−0.24	3.4 ± 0.5
16	0510610201	276	1.85 ± 0.05	3.91 ± 0.21	1.98 ± 0.04	7.60 ± 0.69	0.84	0.23	5.9 ± 0.5
17	0502030101	703	6.38 ± 0.02	10.19 ± 0.08	6.67 ± 0.02	9.60 ± 0.66	0.89	−0.17	2.8 ± 0.6
18	0670920301	673	2.44 ± 0.09	3.84 ± 0.36	2.49 ± 0.09	1.68 ± 0.15	0.77	−0.81	3.1 ± 0.1
19	0670920401	127	10.76 ± 0.11	11.69 ± 0.77	10.78 ± 0.12	1.03 ± 0.07	0.76	−0.21	1.6 ± 0.2
20	0670920501	626	1.64 ± 0.04	3.78 ± 0.17	1.76 ± 0.05	4.91 ± 0.29	0.77	0.15	1.3 ± 0.2
21	0658801301	283	5.97 ± 0.07	9.24 ± 0.18	6.38 ± 0.07	1.92 ± 0.19	0.97	0.05	10.6 ± 0.1
22	0658801801	230	6.13 ± 0.08	14.02 ± 0.34	6.65 ± 0.08	2.74 ± 0.39	0.91	0.57	4.3 ± 0.5
23	0658802301	314	3.16 ± 0.13	3.92 ± 0.51	3.21 ± 0.13	1.64 ± 0.26	0.65	−1.46	6.9 ± 0.4
24	0791780101	76	0.47 ± 0.12	2.21 ± 0.43	0.61 ± 0.11	2.01 ± 0.23	0.18	0.23	0.9 ± 0.2
25	0791780601	420	0.74 ± 0.09	1.09 ± 0.24	0.78 ± 0.08	4.92 ± 0.56	0.46	−0.45	1.1 ± 0.2

Note. Number: the respective figure number; Observation ID; $\bar{x}$: the average photon counts per second for a given observation; F_{var}: the fractional rms variability amplitude for the soft, hard, and total bands; τ_{var}: the variability timescale, derived from the total LC flux; A: the maximum value of the DCF; μ: the time lag at which the DCF peaks; and σ: the width of the fitted Gaussian function. All Observation IDs are arranged in chronological order.

seen in the normalized LCs in the hard- and soft-energy bands, as the rise and fall of the fluxes in both the bands look similar. Higher variability is visible in the hard band, which is similar to the result obtained by Brinkmann et al. (2001). The soft- and hard-band fluxes are well congruent with each other, thus inferring zero lag.

4.1.2. Obs. ID 0099280201

The 40.1 ks observation displays high variability, above 9%, in all the considered energy bands (Table 2). There are three distinct flares visible during the observation. The hard flux precedes the soft and spectral variability, which could possibly contribute to the nonzero lag $\mu = 2.44$ ks observed in the DCF analysis. This is also clearly visible in the the normalized LCs, where we see that after 20 ks of observation, there is a steeper rise in the hard photons compared to the soft photons. A slight loop structure in the clockwise direction is visible in the HR–I diagram at the beginning of the observation, while the overall HR distribution looks pretty flat, without any harder-when-brighter trends.

4.1.3. Obs. ID 0099280301

The photon fluxes measured for this 49.8 ks observation range from 400 to 463, 51 to 84, and 451 to 548 cts s^{-1} for the soft-, hard-, and total-energy bands, respectively. The F_{var} in the hard-energy band is more than three times higher than in the soft- and total-energy bands. In our view, indications (which are not quite clear) of two loops can be traced in the

HR–I diagram, one in the anticlockwise direction, followed by one in the clockwise direction, after around 20 ks of observation. The value of the fitted DCF time lag of −0.19 ks is small. After inspection of panel (e) of Figure 1.3, it is compatible with zero lag.

4.1.4. Obs. ID 0136540101

Just like the previous observations, the variability in the hard-energy band is comparatively very high, while for the soft- and total-energy bands, it is almost equal. The flux ranges from 329 to 423, 28 to 50, and 358 to 471 cts s^{-1} in the soft-, hard-, and total-energy bands, respectively. The derived minimum flux variability timescale is 3.4 ks. This behavior of the variability over short time intervals is also clearly visible in the normalized LCs in panel (e). A nonsignificant time lag of −0.21 ks, derived from DCF fitting, indicates that the soft photons should precede the hard ones, but no such trend can be observed by eye in panel (e). The HR–I plot depicts a clear harder-when-brighter behavior, with embedded looplike structures in the general trend.

4.1.5. Obs. ID 0136541001

The flux is highly variable: from 248 to 284, 22 to 30, and 272 to 313 cts s^{-1} in the energy ranges of 0.3–2.0 keV, 2.0–10.0 keV, and 0.3–10.0 keV, respectively. The time lag of the hard photons derived from the DCF is −1.11 ks, but the Gaussian fitting looks poor, with the peak of the Gaussian not being consistent with the time corresponding to the highest
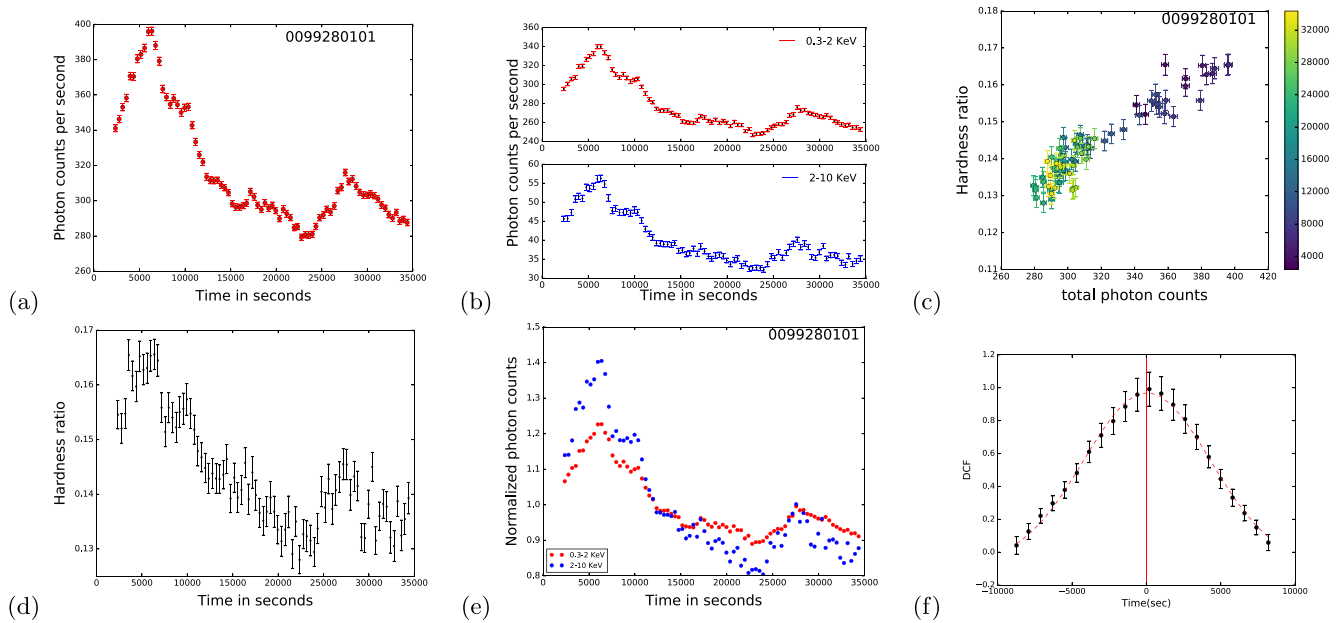
Figure 1. Obs. ID 0099280101. (a) The LC in the total-energy range (0.3-10.0 keV). (b) The LCs in the hard- and soft-energy bands. (c) HR–I diagram. (d) HR vs. time. (e) The normalized LCs in the hard- and soft-energy bands (the points are without error bars for picture clarity). (f) DCF. In panel (c), the observation time (in seconds) is coded by color—dark blue for the beginning of the observation and yellow for the end of observation.

(The complete figure set (25 images) is available.)

DCF value. Inspection of the normalized soft and hard LCs does not provide any clear clues as to where along the LC the DCF delay originates. The HR–I diagram shows only a moderate harder-when-brighter trend. Also, the HR forms an anticlockwise loop with respect to time in the HR–I plot.

Ravasio et al. (2004) analyzed only the flaring part of this observation, and they reported a clockwise loop in the HR–I diagram. This is an interesting case, as we see an anticlockwise loop formation in the HR–I diagram for the entire observation. We have plotted HR–I diagrams for both the cases, the flaring part and the whole LC, in panel (i). The reversal of the loop is an interesting behavior that is revealed in this observation.

4.1.6. Obs. ID 0158970101

This 47.5 ks observation depicts flux ranging from 282 to 327, 18 to 26, and 302 to 399 cts s^{-1} in the soft-, hard-, and total-energy bands, respectively. The fractional variability in the soft- and total-energy bands is almost equal, while it is higher by 2% in the hard-energy band. From the DCF, there is a clear positive lag in the observation of 2.56 ks, suggesting that the emission of hard-energy photons precedes the emission of soft-energy photons. This is also very evident in the normalized LC, with the visible shift of the hard- and soft-energy bands. In the HR–I diagram, one can clearly see a clockwise loop, but apparently there is no harder-when-brighter trend in the data.

4.1.7. Obs. ID 0150498701

This 49.3 ks observation has clearly variable flux ranges, from 483 to 714, 52 to 92, and 536 to 808 cts s^{-1} in the soft-, hard-, and total-energy bands, respectively. The amplitude of the fractional variability of this observation is approximately 8% in both the soft- and total-energy bands, while it is much

higher and almost double, with a value of 17.61%, in the hard-energy band.

There is a lag in the soft photons of 1.71ks, calculated from the Gaussian fitting on the DCF, but this is not clearly visible in the normalized LCs. The HR–I diagram shows a clear harder-when-brighter behavior, and forms a loop in the clockwise direction over time.

4.1.8. Obs. ID 0162960101

This is a 50.7 ks observation, with the flux ranging from 305 to 343, 32 to 41, and 339 to 381 cts s^{-1} in the soft-, hard-, and total-energy bands, respectively. There are relatively low variability amplitudes, with small differences between the energy bands (2.79% for soft, 4.62% for hard, and 2.91% for total), but the fractional variability in the hard state is still significantly larger than those in the other bands. The derived minimum flux variability timescale is 2.61 ks.

The time lag is 0.04 ks, which is a very small positive lag. The HR–I diagram looks scattered, with no HR variation with flux or time.

4.1.9. Obs. ID 0158971201

This 66.1 ks observation has the highest flux, as can be seen from the LCs. The flux values in the total-energy band go as high as 1073 cts s^{-1}, and the lowest flux value for this observation is approximately 691 cts s^{-1}. The flux ranges from 86 to 224 cts s^{-1} in the hard-energy band, and from 603 to 856 cts s^{-1} in the soft-energy band. This observation also shows the highest amount of flux variability, with an amplitude in the hard state of 22.85%, while in the soft- and total-energy ranges it is around 10%. From the Gaussian fitting to the DCF, the time lag is calculated to be −0.38 ks. The HR–I diagram shows a complex structure, consisting of multiple vertically shifted branches, with a clear harder-when-brighter trend in the full

observation, as well as in each individual branch. The HR is also highly varied over time, reaching the highest value of 0.26 of all the observational series analyzed.

4.1.10. Obs. ID 0153951201

This 10.0 ks observation, the shortest observation in our set, is characterized by flux ranges from 564 to 652, 58 to 73, and 623 to 725 cts s^{-1} in the soft-, hard-, and total-energy bands, respectively. The fractional variability amplitude is between 4% (for the soft and total bands) and 6.5% (for the hard band).

The time lag as calculated from the Gaussian fitting of the DCF is small, with a positive value of 0.23 ks. From the plots in Figures 10(e) and (f), this lag is very small, and it can be considered as zero lag. The HR–I diagram does not show any clear structure, only showing a slight harder-when-brighter trend.

4.1.11. Obs. ID 0158971301

This 60.0 ks observation has a high range of flux, of 551–797, 68–120, and 623–912 photon counts per second, in the soft-, hard-, and total-energy bands, respectively. A flare is also visible in the LC between 30 and 50 ks of the observation, with the hard component preceding the soft one. In all three energy bands, this observation has a high fractional variability amplitude of above 10%. The time lag in the DCF fit is 1.31 ks, showing that the hard photons precede the soft ones. The HR increases with increasing flux, and forms clockwise loops over time along the general trend.

4.1.12. Obs. ID 0302180101

This 41.9 ks observation has flux ranges from 443 to 517, 53 to 76, and 498 to 594 cts s^{-1} in the soft-, hard-, and total-energy bands, respectively, and shows modest fractional variability of 4%, for the soft- and total-energy bands, with the value being almost double in the high band. This is the observation with the longest minimum timescale of flux variation, of 10.59 ks, in our set of studied observations. The DCF time lag between the hard and soft state is 0.90 ks. The HR–I diagram forms a slightly complex structure with respect to time, showing an average harder-when-brighter trend, as can be in seen in Figure 1.12 (panels (c) and (d)). It is interesting to note that, in panel (e), the minima of the LCs in the soft and hard bands are similar within the given bands, but much different between the bands.

4.1.13. Obs. ID 0411080301

This 69.2 ks observation has the largest average flux count in our set of data, with the flux values in the soft-, hard-, and total-energy bands ranging from 643 to 753, 109 to 150, and 752 to 902 cts s^{-1}, respectively. The fractional variability amplitude in the hard-energy band is almost double the values for the soft- and total-energy bands. There is a slight (nonsignificant) positive lag between the hard- and soft-energy bands, of 0.31 ks. The HR–I diagram depicts a trend supporting harder-when-brighter behavior. The HR is highly variable with respect to time, and does not form any visible loop structure.

4.1.14. Obs. ID 0411080701

This 18.9 ks observation has small variability amplitude. The flux ranges from 276 to 289, 18 to 21, and 295 to 309 cts s^{-1} in

the soft-, hard-, and total-energy bands, respectively. There is a negative time lag of −0.94 ks, which means that the soft-energy photons precede the hard-energy photons. This lag is clearly visible in the DCF plot (panel (f)), but it is not particularly evident when inspecting the normalized LCs in panel (e). In the HR–I diagram, panel (c), a looplike structure can be noted, but the average spectral hardening with increasing flux is quite weak.

4.1.15. Obs. ID 0510610101

This 27.6 ks observation has flux ranges of 244 to 256, 14 to 16, and 259 to 273 cts s^{-1} in the soft-, hard-, and total-energy bands, respectively. Just like the previous observation, this one also has a low fractional variability amplitude, with values of less than 1.5% in the soft- and total-energy bands. The value of the variability amplitude in the hard-energy band is 3.36%. The derived minimum flux variability timescale is 4.69 ks. A negative lag of 0.24 ks is fitted to the DCF. The HR–I diagram looks relatively flat.

4.1.16. Obs. ID 0510610201

This is a 22.7 ks observation, with the flux ranging from 250 to 267, 15 to 17, and 265 to 284 cts s^{-1} in the soft-, hard-, and total-energy bands, respectively. The small fractional variability amplitude is less for the soft- and total-energy bands, but 3.91% for the hard-energy band. There is a positive lag of 0.23 ks between the hard and soft photons, obtained from the Gaussian fitting to the DCF. This slightly positive lag is clearly visible in the DCF plot. The HR–I plot is quite flat, and does not show any particular structure over time.

4.1.17. Obs. ID 0502030101

This is a 43.2 ks observation, with the flux ranging from 594 to 749, 47 to 73, and 642 to 822 cts s^{-1} in the soft-, hard-, and total-energy bands, respectively. The LC shows a nearly monotonic decrease throughout the observation. The flux variability amplitude of this observation in the soft- and total-energy bands is around 6.5%. In the hard-energy band, the F_{var} value is 10.19%. The observation has a relatively long minimum flux variability timescale of 9.60 ks. This observation also shows a negative lag in the DCF, with the emission of soft photons preceding the emission of hard photons by 0.17 ks. From the plot of the Gaussian fitting over the DCF, this lag appears to be quite small, and it can be considered as no lag. The HR–I diagram shows a nonmonotonic harder-when-brighter behavior, without forming any loop structure.

4.1.18. Obs. ID 0670920301

This short 16.2 ks observation presents flux variations from 605 to 655, 41 to 48, and 646 to 702 cts s^{-1} in the soft-, hard-, and total-energy bands, respectively. The LC shows the flux to be regularly decreasing over time. The fractional variability amplitude in all three energy bands is around 3%. The derived minimum flux variability timescale is quite short. According to the DCF fit, the soft-energy photons precedes the hard-energy photons, by 0.81 ks. The HR variability with respect to both flux and time is flat, without any regular trends, and no loop structures are visible in the HR–I diagram.

4.1.19. Obs. ID 0670920401

This short 18.0 ks observation depicts a low, continuously decreasing flux, ranging from 104 to 152, 4 to 7, and 109 to 159 cts s^{-1} in the soft-, hard-, and total-energy bands, respectively. The fractional variability amplitude is really high in all energy bands, with values slightly above 10%, which may possibly have been boosted by measurement errors. This is the observation in which the lowest value of the minimum variability timescale is calculated, with a value of 1.03 ks. From the Gaussian fitting to the DCF, there is a negative lag of 0.21 ks. The HR–I diagram is clearly flat, with very low values of HR.

4.1.20. Obs. ID 0670920501

The LC of this short 18.0 ks observation shows variations from 550 to 590, 45 to 52, and 597 to 642 cts s^{-1} in the soft-, hard-, and total-energy bands, respectively. The fractional variability amplitude is below 4% in all three energy bands. A very small positive lag of 0.51 ks is visible in the DCF between the hard- and soft-energy photons. The HR–I diagram shows a slight increase in the HR with increasing flux.

4.1.21. Obs. ID 0658801301

This 29.0 ks observation has flux ranges of 225–270, 31–43, and 256–312 cts s^{-1} in the soft-, hard-, and total-energy bands, respectively. The fractional variability amplitudes are 6% in the soft- and total-energy bands, while in the hard-energy band it is 9.24%. From the DCF plot, it can be said that the time lag is consistent with zero. The HR shows a weak harder-when-brighter trend.

4.1.22. Obs. ID 0658801801

In the regularly growing LS of this 33.6 ks observation, one can see the flux ranging from 196 to 243, 11 to 19, and 208 to 262 cts s^{-1} in the soft-, hard-, and total-energy bands, respectively. The existing harder-when-brighter behavior is nicely illustrated by the normalized LCs in panel (e), with the rise in the hard-band flux being steeper than the rise in the soft band. The fractional variability amplitude in the hard-energy band is pretty high, with a value of 14.02%, compared to the values in the soft- and total-energy bands, which are around 6.4%. The fitted positive lag in the DCF is 0.57 ks, but in reality there may be no lag for this nearly monotonic changing LC.

4.1.23. Obs. ID 0658802301

This 29.4 ks observation has flux ranges of 279 to 312, 17 to 23, and 298 to 334 cts s^{-1} in the soft-, hard-, and total-energy bands, respectively. This observation has low fractional variability amplitudes of 4% in the three energy bands. The minimum variability timescale is 1.64 ks. There is a significant negative time lag in the DCF, with the soft-energy photons preceding the hard-energy photons, by 1.46 ks. However, such a delay is not visually pinpointed in the plot of the normalized LC, due to the large scatter in the hard band. The HR–I diagram does not show any trend with the flux.

4.1.24. Obs. ID 0791780101

This 17.5 ks observation is characterized by very small flux and is classified with our selected conditions as being nonvariable. In the data, the flux points range from 69 to 72, 5 to 6, and 75 to 78 cts s^{-1} in the soft-, hard-, and total-energy bands, respectively. The normalized LC of the hard band is only more scattered than the soft band, without any common trends between them. The fractional variability amplitude is around 0.5% in the soft- and total-energy bands, and 2.21% in the hard-energy band. It is not easily understood how the formally derived minimum flux variability timescale for this case is so small a value as 2.01 ks. The HR evaluated for this observation also does not show variability in time, but a small growth trend with flux is not excluded. The DCF has been calculated and a Gaussian fitting has been done for this observation, like all the other observations, but they show negligible signs of correlated variability between the bands. However, a small nonzero maximum near zero lag, with $A \approx 0.2$, suggests a small contribution of flux variability to the data scatter, due to measurement errors.

4.1.25. Obs. ID 0791780601

This very short 12.5 ks observation is the second of the two observations classified by our selected conditions as being nonvariable. The measured flux point ranges for this observation in the soft-, hard-, and total-energy bands are 357 to 371, 55 to 59, and 414 to 430 cts s^{-1}, respectively. The fractional variability amplitude in the hard-energy band is 1.08%, while in the soft- and total-energy bands it is below 0.8%. From the DCF Gaussian fitting, one finds a maximum with $A \approx 0.4$ and a time lag of -0.45 ks. In the normalized LCs, a correlation between the hard- and soft-energy bands is evident. Thus, some small variability must be present in these data, contrary to our classification. The HR plots with respect to flux and time do not show any regular trends.

4.2. Flux Variability

For all 25 EPIC-pn XMM-Newton pointed X-ray observations, we study the LCs in the soft- (0.3–2.0 keV), hard- (2.0–10.0 keV), and total- (0.3–10.0 keV) energy bands, as presented in Figure 1 (the complete set of plots is provided in the online figure set). Below, we describe some observed general trends and findings from the analysis.

On visual inspection, we notice that all the LCs in the total-energy band show substantial (23 observations) or weak (two observations) flux variations on IDV timescales. To quantify these visual findings, we derived the fractional rms variability amplitude F_{var}, using Equation (4), and the minimum two-point variability timescale τ_{var}, using Equation (6), for all the individual Observation IDs. The results are provided in Table 2. To make sure of the dependence of F_{var} on the flux, the two parameters are plotted in Figure 2(c), for which the Spearman rank correlation was evaluated to be 0.25. This shows a weak dependency of F_{var} on the flux. $F_{var}(total)$ and $F_{var}(soft)$ have a Spearman rank correlation and a Pearson correlation of approximately 0.5 with observation duration, while $F_{var}(hard)$ and observation duration have a Spearman rank correlation and a Pearson correlation of approximately 0.6 (Figure 2(a)). These show that the F_{var} in the different energy ranges have a moderate dependency on the duration of the observation.
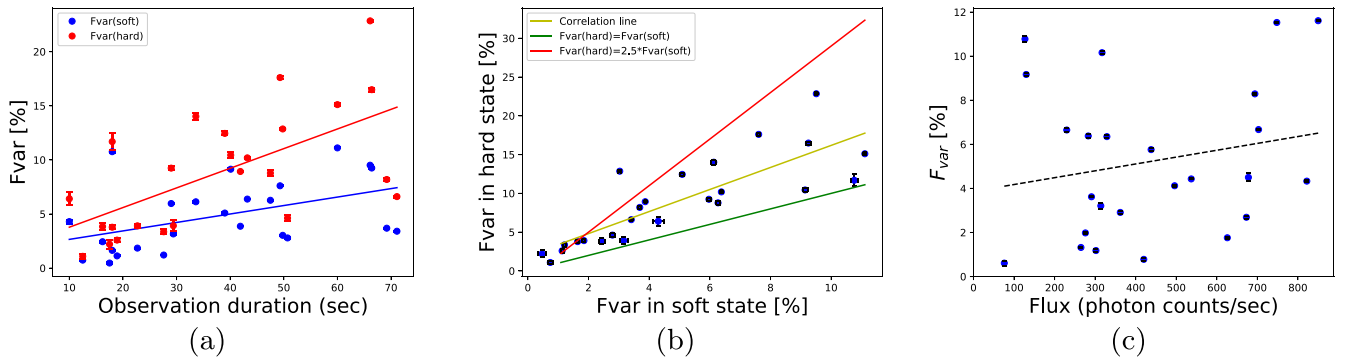
Figure 2. (a) Fractional variability $F_{\rm var}$ in the soft- and hard-energy bands plotted vs. the duration of the observation; fitted correlation lines are provided for both distributions. (b) $F_{\rm var}$ in the hard vs. the soft bands. The lines $F_{\rm var}({\rm hard}) = F_{\rm var}({\rm soft})$ and $F_{\rm var}({\rm hard}) = 2.5 F_{\rm var}({\rm soft})$ are provided for reference. (c) $F_{\rm var}$ in the total-energy band vs. flux, with the correlation line represented by the dashed line

The often applied condition for source variability, $F_{\rm var}$ being greater than $3 \times (F_{\rm var})_{\rm err}$, leaves only two Observation IDs, 0791780101 and 0791780601, as being nonvariable. All 23 of the other observational runs satisfy this condition for variability. Substituting these results into Equation (12), we have estimated the source DC in the total-energy range (0.3–10.0) keV. Of the 25 pointed observations, 23 showed variability on IDV timescales, yielding the DC as 96%. $F_{\rm var}$ $> 3 \times (F_{\rm var})_{\rm err}$ is not the only criterion for judging variability in LCs, and failing this criterion does not necessarily mean that the source is not variable. It is also possible to fail to meet the criterion due to a low photon count or a shorter time duration. Let us note that with a visual inspection of the "nonvariable cases," ID 0791780601, presented in Figure 1.25, shows some level of variability, both from a visual inspection of the LC and from the derived DCF shape, with a maximum correlation close to zero delay between the hard and soft LCs. Such a correlation should not appear from the fluctuations in a subband of the source emission with constant flux. For the second "nonvariable" observation, ID 0791780101 (Figure 1.24), hardly any clear signatures of variability can be pinpointed in the LC, but an inspection of the DCF plot again shows a small maximum, indicating a weak hard/soft correlation close to zero time delay, which could be considered as suggesting a weak variable signal being added to the LC fluctuations due to measurement errors, in agreement with the red-noise behavior of Mrk 421. Therefore, the above DC value should rather be considered as the lower limit, with a possible DC = 98.6%, or even 100%, if one believes our argument supporting a small amplitude variability in the LC of Observation ID 0791780101. For these reasons, we present all Observation IDs with plots of the variability parameters. Our result here is consistent with the Mrk 421 DCs of 100% and 84% that were found using observations from Suzaku and Chandra, respectively (Aggrawal et al. 2018; Zhang et al. 2019).

The largest fractional variability amplitude in the total-energy band studied is 11.6%, for ID 0158971201, while the minimum of $F_{\rm var} = 0.61\%$ is derived for ID 0791780101. When analyzing the variabilities in our selected hard and soft bands, we note the interesting trends presented in Figure 2. $F_{\rm var}({\rm soft})$ and $F_{\rm var}({\rm hard})$ are highly correlated with each other, with a Spearman rank correlation of approximately 0.9 and a Pearson correlation of 0.82. For each plot in Figure 2, the correlation line is plotted using Pearson correlation values. When analyzing the figure, one should note that particular points in the presented distributions depend on our arbitrary

split at 2 keV of the total band into two energy bands. This choice, characterized by having a majority of photons in the soft band, leads to our HR values being much smaller than 1, and the variabilities of the total flux being very close to the soft-band variability. Thus, the distribution of $F_{\rm var}({\it total})$ is nearly identical to the one for $F_{\rm var}({\it soft})$, with $F_{\rm var}({\it total})$ always being slightly greater than $F_{\rm var}({\it soft})$, so we decided not to show it on the plot, for picture clarity. In Figure 2, one may note that the variabilities in the more energetic band are higher than the ones in the lower-energy band, but also that, on average, in each energy band $F_{\rm var}$ grows with observational time duration (Figure 2(a)), due to longwave LC fluctuations providing additional power in the long observation runs. In panel (b) of the figure, we compare the values of the variabilities in both energy bands, showing that in all the observations studied the variabilities in the hard band are substantially higher than the variabilities in the soft band, but for the large majority of cases $F_{\rm var}({\it hard}) < 2.5\, F_{\rm var}({\it soft})$. The limits are as follows. For the soft band, $F_{\rm var}$ ranges from 0.47% to 11.11% for observations 0791780101 and 0158971301, respectively, while in the hard band it ranges from 1.09% for observation 0791780601 to the value of 22.85% for observation 0158971201.

The extensively discussed relation here, between the hard and soft bands, is not very new in the literature. Peretz & Behar (2018) classified AGNs on the basis of X-ray variability, and reported that for the RL AGNs, the variability is dominated by the variability in the hard band over the variability in the soft band. Brinkmann et al. (2001) also pointed this out for one observation of Mrk 421 from the XMM-Newton satellite. Also, the discussion of the blazar power spectra in different energy bands by Goyal (2020) demonstrates the domination of high-energy variability at short IDV timescales for X-ray and γ-rays over optical and radio variabilities.

The minimum variability timescale in the analyzed observations ranges from 10.59 to 1.03 ks, the longest being for observation 0302180101, and the smallest for observation 0670920401. To study the relation of $\tau_{\rm var}$ with the activity state of the source, which is measured here by the mean flux for a given Observation ID, we have plotted in Figure 3(a) $\tau_{\rm var}$ against the mean flux for each observation. The distribution is highly scattered, without any clear trend. To help with the evaluation, we also provide a dashed curve (arbitrarily normalized) showing the expected relations for the same time bins used in all observations, and by assuming the same characteristic maximum flux change between two successive data points in all observations. In Figure 3(b), a quite
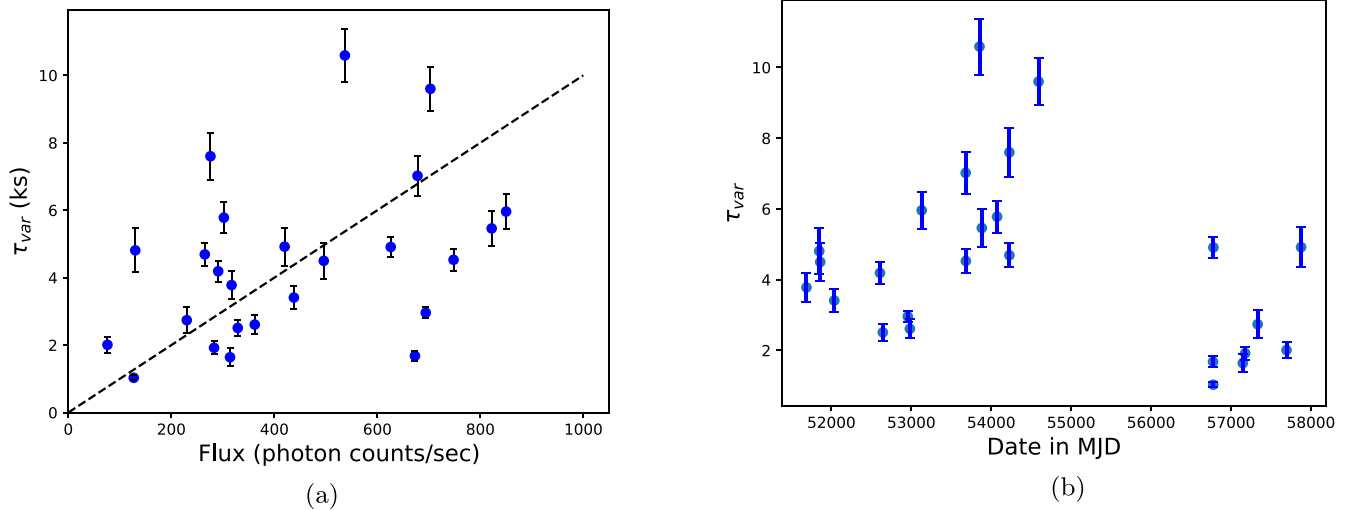
Figure 3. (a) A plot of $\tau_{\rm var}$ vs. the mean photon flux $\bar{x}$ for all observations. An arbitrarily normalized dashed line $\tau_{\rm var} = 4$ ks $\times$ Flux/(400 cts s^{-1}) is provided for reference, showing the expected $\tau_{\rm var}$ values for the same Δx and Δt used in all data sets. (b) The minimum variability timescale $\tau_{\rm var}$ plotted against the observation dates, given in modified Julian date, for all observations.
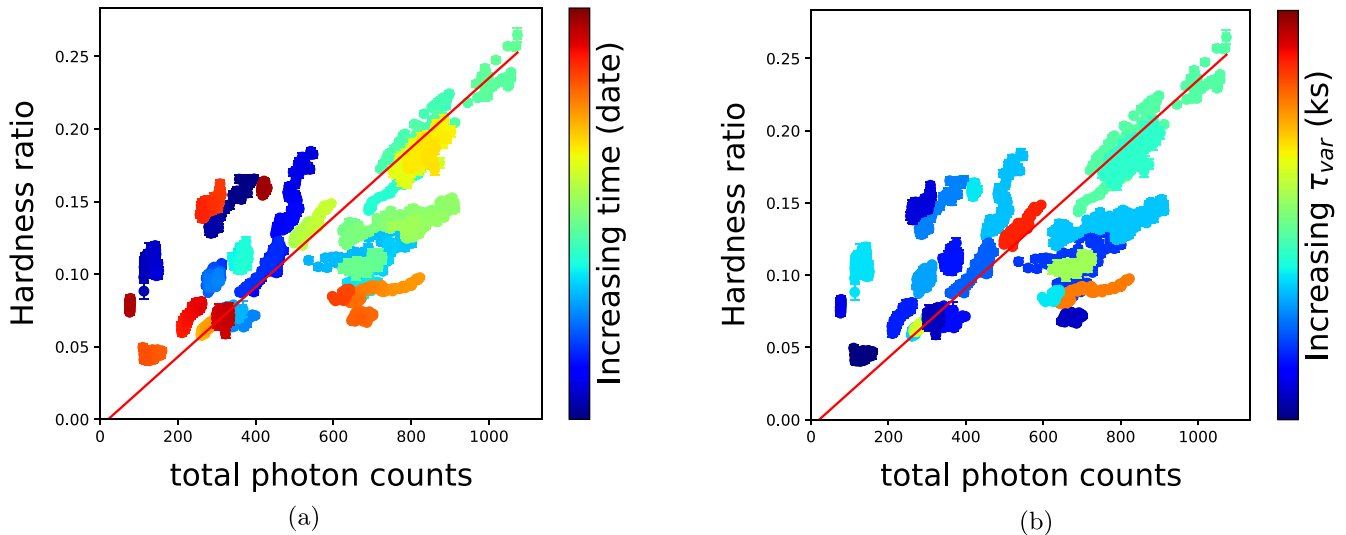

Figure 4. HR–I diagram of all the plots combined into one, with the color bar (a) depicting the chronology of the observation, from the first observation taken on 2000 May 25 to the last observation taken on 2017 May 4, and (b) showing the distribution of the derived $\tau_{\rm var}$ within the observations.

interesting structure of $\tau_{\rm var}$ changes over 17 yr, when the date of observation is observed. One should note the significant regularity of these changes in the plot, where the scatter in $\tau_{\rm var}$ is quite limited over small time ranges, but it significantly evolves up and down over the observational period. In our opinion, the observed nonrandom structure reflects regular physical changes in the blazar emission zone.

4.3. Spectral Variability

4.3.1. Hardness Ratio

The harder-when-brighter behavior is claimed to be a general property of HBL/HSP blazars (e.g., see Gupta 2020 for a review). The observations here show more or less regular trends, with at least half of the observations exhibiting the harder-when-brighter behavior, but also including various zigzags with short vertical evolution paths or, on average, a constant value of HR. To compare these structures for all Observation IDs, we present an HR–I summary diagram for all

observations in Figure 4, with a color bar representing the chronology of the presented data. In the plot, one can note a general harder-when-brighter trend, which we fit with a reference red line, but the structure seems to be more complicated. This red line is the line of best fit, which was obtained using the eyeball method. If the line presents a reference trend for the source, then we note that at lower count rates, below 500 cts s^{-1}, all the data sets are situated above or extend from the reference line to higher HRs. On the other hand, for the higher count rates, the HR–I distributions extend along the reference line or extend from the line to lower HRs.

It is important to note that in many Observation IDs, looplike structures are observed at HR–I plots, with both clockwise and anticlockwise evolutions in time. Occasionally, both these orientations occur in a single observation. The Observation ID 0136541001 (Figure 5), taken on 2000 December 1, forms an overall clockwise loop in the HR–I diagram. But when choosing only the flaring part of the LC, the HR–I diagram depicts an anticlockwise loop. This is in agreement with
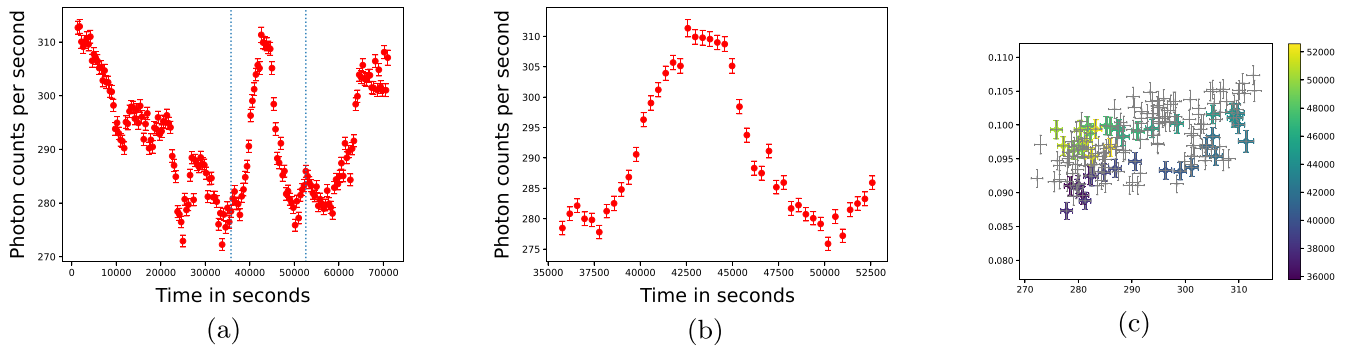
Figure 5. Obs. ID 0136541001. (a) The LC with the considered flare marked by the vertical lines. (b) The LC of the flaring part. (c) HR–I diagram of the flaring portion of the LC, plotted in color over the whole LC (plotted in gray) HR–I diagram (Figure 1.5, panel (c)), with a colorbar showing increasing time in seconds.
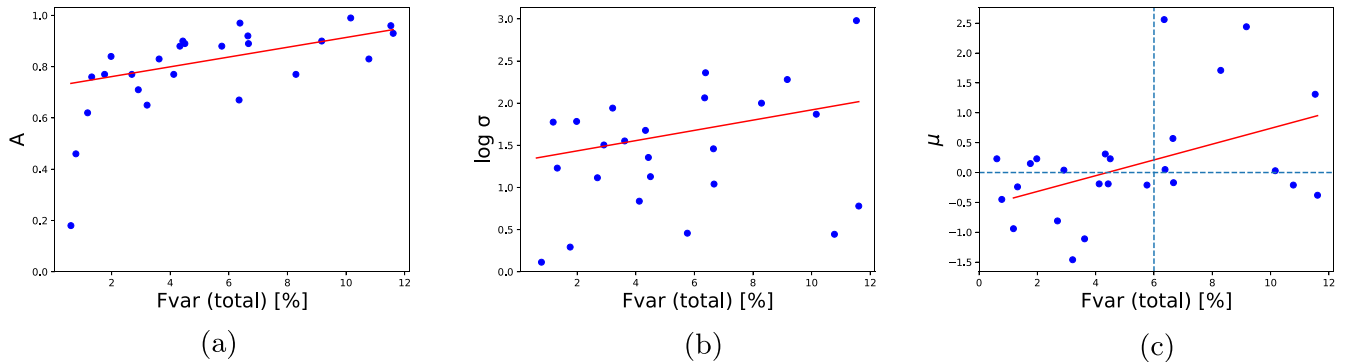

Figure 6. Fractional variability F_{var} vs. the parameters of the Gaussian fits of the DCF maximum. (a) The amplitude A. (b) The width σ. (c) The time lag μ. The red lines represent linear fits to the presented distributions, without considering the two "nonvariable" outliers with the lowest F_{var}. The dashed lines in panel (c) are for a reference, as explained in the text.

Ravasio et al. (2004), who showed an anticlockwise loop for the flaring part of the HR–I diagram. This interesting behavior depicts the complexity of the emission processes. We note that observations forming a loop structure accompany a time lag in the hard-energy or soft-energy photons, as calculated from the DCF fitting, which is further discussed in the next section.

4.3.2. Discrete Correlation Function

All the maxima in the DCF plots (Figure 1, its online elements, and Figure 6) have been fitted with the Gaussian function given by Equation (11), with the fitted parameters presented in Table 2. These parameters have then been tested for correlations (or for nonrandom trends) with respect to the F_{var} values in the total-energy band (see Figure 6). Additional information resulted from the study of the variations of the HR with respect to the flux intensity in the HR–I diagrams in Figures 1.7–1.8 and from the combined HR plots of all observations in Figure 4. The relation of another physical parameter characterizing the emission in each observation, also given in Table 2, was compared to the photon flux as shown in Figure 3(a) and its evolution with time in Figure 3(b).

Ravasio et al. (2004) noted that the DCF is not a robust way of predicting the lag in cases of highly variable LCs. While they dealt with only the flaring parts, in which the LCs were more or less symmetrical in time, we deal with LCs with durations of more than 10 ks, which are often nonuniform and might consist of many flares or longer rise or decline trends. Thus, to understand the features in the LCs responsible for the observed DCF lags in Figure 1 and the online figure set, we directly visually compare the normalized soft and hard LCs, to reveal patterns or shifts between the fluctuating fluxes in order

to understand the origin of the eventually occurring nonzero time delays, μ, appearing in the DCF analysis. A superposition of the various lags in individual flares may lead to zero lag, as also claimed by Ferrero et al. (2006). A positive value for the lag means that the emission of photons in the soft-energy band is delayed with respect to the emission in the hard band, and it is also called a "soft lag." When soft-energy photons precede the emission of hard-energy photons, then μ is negative and the lag is called a "hard lag."

Let us present the main conclusions from these studies of DCFs and from the comparison of the respective *normalized* LCs:

1. There is no statistical preference for a hard lag or a soft lag in the observations under study, with soft lags being observed in 13 observations and hard lags in 11 observations. The lag parameter μ for the observation 0791780101 is not taken into consideration, because not enough data points were available for the DCF modeling.

2. In our 25 observations, we do not notice a preference for lag in a particular energy band in the LCs, but involved LC irregularities could mask small trends, if present. Occasionally, we note a situation with the hard-band variation preceding the soft-band one, or the contrary, and in most cases this is always limited to a fraction of the entire observation. There are observations in which the trend of the rise and fall in the LCs is similar in the two energy bands, as observed in Observation IDs 0099280101, 0099280301, 0136540101, 0136541001, 0158971301, 0302180101, 0411080301, 0510610201, 0670920401, 0658801801, and 06588012301. There are cases of individual flares with regular shapes in both bands

showing no lag between frequencies, as observed in Observation IDs 0099280101, 0136540101, 0162960101, 0158971201, 0158971301, 0302180101, 0411080301, 0510610201, and 0658801301. Also, there are cases in which the trends of the LCs in the two energy ranges are similar in part of the observation, while there is a delay in the rise or fall of the photon counts in the other parts of the LC in either of the energy bands, as in Observation IDs 0099280201, 0158970101, 0162960101, 0411080701, 0502030101, and 0670920501.

3. The registered larger time shifts μ of the DCF maxima may be related to different evolutions on longer timescales of the photon fluxes in the different energy bands, and such observations are also accompanied by the occurrence of looplike structures in the HR–I plots. Such behavior is observed in Observation IDs 0150498701, 0158970101, 0158971201, 0158971301, and 0136541001, and there are indications of a loop forming in observations 0099280201 and 0658802301. All the observations exhibiting clockwise loops in the HR–I diagrams are characterized by soft lags and, on the contrary, there are hard lags in the observations exhibiting anticlockwise loops, as earlier observed in HBLs by Zhang et al. (2002, 2006) and Fossati et al. (2000a). But not all of the observations in our data sample showing positive or negative lags are accompanied by recognizable loops in the HR–I diagrams.

4. In Figure 6, the Gaussian fitting parameters of the DCF maxima are plotted to study their relation with F_{var}. Amplitude A is moderately correlated with F_{var}, with a Spearman correlation coefficient of approximately 0.7. Linear fits to these distributions are added, to illustrate a general trend in each panel. In panel (a), a moderate trend of the DCF maximum amplitude A growing from 0.6–0.8 to 0.7–0.95 is observed when F_{var} grows from 1% to the maximum of 12% (note that the two outliers with the smallest F_{var} were excluded from the fits here and in the two other panels of this figure). A similar but very weak trend, with a Spearman correlation coefficient of 0.3, is observed for the width σ of the fit in the panel (b).

5. In Figure 3(c), one may note a clear systematic trend of large negative or positive DCF lags between the two energy bands with respect to F_{var}. Inspection of this largely scattered plot reveals an interesting structure, with all the extremely negative (down to < -1.5 ks) μ values occurring only at low variabilities, $F_{var} \leqslant 4\%$, while above 6% all the μ values deviating significantly from zero appear to the positive side, reaching up to $+2.5$ ks. Fisher's exact test was applied to our null hypothesis that the two parameters DCF lag and F_{var} are independent of each other. The calculated Fisher exact statistics value is 0.2, and the null hypothesis is accepted. Thus, based on this test, we cannot prove our speculation of the dependency of positive or negative lag on the extent of the variability. But, on the other hand, there is a moderate correlation between DCF lag and F_{var}, with a Spearman correlation coefficient of 0.4, depicting a relation between large negative lags with low F_{var} and high positive lags with high F_{var}. Thus, a lag in soft photons is more often observed in more variable observations, while a lag in hard photons is dominant for low X-ray variabilities.

5. Conclusions

In the present paper, we reanalyzed a rich sample of 25 observations of TeV blazar Mrk 421 X-ray emission, with the EPIC-pn instrument on board XMM-Newton, attempting to conduct a detailed multiparameter study of the individual observations, as well as to compare the relations of the derived parameters for the full set of observations. We used the obtained IDV LCs to study the flux and spectral variations. Particularly interesting information was extracted from a comparison of the soft and hard X-ray subband variability properties, by studying HR from the emission in the two subbands, the DCF, and by comparing the normalized LCs in both energy bands. Verification of the accompanying HR–I diagrams and the trends observed between them, as well as the trends in the derived minimum variability timescales for all data sets, gave additional perspective to the study. Without simultaneous MW data, besides making a few speculations, we did not intend to model the studied emission processes, but rather we revealed the significant constraints for any such modeling from a detailed single–frequency band study to conclude that:

1. The fractional variability displays clear evidence of large amplitude IDV in most of the Observation IDs (23 of the 25 considered X-ray (sub)bands). We found the IDV DC to be 96%, but some level of variability is noted in all the data.

2. The fractional variability amplitude depends on the studied X-ray energy range, and it is always higher in the hard band than in the soft band (and in the total-energy band). In the great majority of the studied cases in the energy band we selected, the fractional variability in the hard band is from ≈ 1 to 2.5 times higher that the variability in the soft band.

3. The total-energy-weighted minimum variability timescales for all Observation IDs occur in the range from 1.03 to 10.59 ks. We note that this scale is not randomly distributed, but subject to regular trends over the 17 yr of observations, possibly indicating regular underlying changes in the physical conditions of the emission zone (like shifts of the emission zone along the jet, changing the magnetic field).

4. The measured time lags between the (0.3–2.0) keV (soft) and (2.0–10.0) keV (hard) bands from the DCF maximum fitting do not reveal any constant pattern. In the majority of cases, a very small time lag occurs, while when inspecting the normalized LCs in the hard- and soft-energy bands, one can see the positive, negative, or unclear pinpointing of lags in the different structures observed along the LCs. We also note that the occurrence of longtime trends between the studied energy bands results in the time lags derived in the DCF analysis, even if short individual flares in the hard and soft subbands perfectly coincide in time.

5. The HR analysis for our soft versus hard bands shows a similar pattern as the LCs for most of the Observation IDs, with the emission in the hard-energy band always being more variable than in the soft band, and the harder-when-brighter average trend of HSP blazars being confirmed in the majority of the observations of Mrk 421.

6. In numerous observations, one may note the formation of clockwise and anticlockwise loops in the HR–I diagrams.

We observe the interesting feature of the change in direction of the loop in the HR–I diagram for the short-time flare with respect to the loop appearing in the entire observation of 0136541001. One may note that Zhang et al. (2006) attempted to explain the directions of such loops on the basis of the energy-dependent acceleration and cooling timescales of the emission particles, by somewhat arbitrarily varying these parameters for hard and soft photons. We prefer to think about the possible physical sources of such observations, relating to the complexity of the relativistic magnetic field reconnection regions and the relativistic turbulence within the jet volume modulated by the fluctuating jet density (or shocks).

7. We observe that the occurrence of the big lags in soft or hard photons is moderately related to the degree of flux variability. There are large negative lags (soft photons leading) in less variable observations, while highly variable observations have shown large positive lags (hard photons leading). We also see in our data set that the observations forming a clockwise loop in the HR–I diagram have a positive time lag, while those forming an anticlockwise loop have a negative lag.

In our opinion, the observations with the described trends or correlations clearly oppose the application of shock acceleration mechanisms for the explanation of blazar synchrotron emission in the X-ray range. In shocks, high-energy particles require longer times for acceleration, and our observed events with the high-energy emission preceding the low-energy one are in contradiction to such a model. Also, in the flares generated by shocks, some degree of regular asymmetry between the rising and declining parts of the flare is to be expected, which is not observed in the data. Of course, the shock could still be a modulating factor through its compressive effects for some other acceleration and emission processes occurring in the medium, but even such an influence should be reflected in some systematics in the observations, which we do not pinpoint here. So, even without referring to MW observations, we suggest that processes involving (relativistic magnetohydrodynamics) turbulence are required to explain the considered X-ray data contrary to one zone. This is contrary to the earlier usage of one zone (Böttcher & Dermer 2010) and two zone (Błażejowski et al. 2005) for the modeling of blazar spectra.

Similar questions can be asked when postulating magnetic field reconnection processes as the emission sources. In such a situation, one could imagine the hard band preceding or being delayed with respect to the soft-band emission, but the symmetry of some individual flares is still difficult to explain if the reconnection is not modulated by an external symmetric process. In our view, such models could fit the varying emission details in different observations if the emission is generated by a modulated ensemble of numerous reconnection processes operating with timescales much shorter than the flares we observe. Fluctuating Lorentz factors within the jet would further complicate the situation.

Of course, any model intending to explain blazar emission should be verified with simultaneous MW observations. However, any such verification should consider (as far as possible) IDV timescales, where individual emission acts can give insights into the physics of acceleration processes. As a rule, there are significant numbers of free parameters in the blazar emission models, and one should be careful when making any real physical modeling, if it is not limited to playing with the free parameters only.

ORCID iDs

A Priyana Noel ● https://orcid.org/0000-0002-1568-6127
Haritma Gaur ● https://orcid.org/0000-0002-6629-8490
Alok C. Gupta ● https://orcid.org/0000-0002-9331-4388
Alicja Wierzcholska ● https://orcid.org/0000-0003-4472-7204
Michał Ostrowski ● https://orcid.org/0000-0002-9199-7031
Vinit Dhiman ● https://orcid.org/0000-0002-8105-4566
Gopal Bhatta ● https://orcid.org/0000-0002-0705-6619

References

Abeysekara, A. U., Albert, A., Alfaro, R., et al. 2017, ApJ, 841, 100
Acciari, V. A., Aliu, E., Arlen, T., et al. 2011, ApJ, 738, 25
Acciari, V. A., Ansoldi, S., Antonelli, L. A., et al. 2020, ApJS, 248, 29
Agarwal, A., Gupta, A. C., Bachev, R., et al. 2016, MNRAS, 455, 680
Aggrawal, V., Pandey, A., Gupta, A. C., et al. 2018, MNRAS, 480, 4873
Aleksić, J., Ansoldi, S., Antonelli, L. A., et al. 2015a, A&A, 576, A126
Aleksić, J., Ansoldi, S., Antonelli, L. A., et al. 2015b, A&A, 578, A22
Barth, A. J., Ho, L. C., & Sargent, W. L. W. 2003, ApJ, 583, 134
Bhagwan, J., Gupta, A. C., Papadakis, I. E., & Wiita, P. J. 2014, MNRAS, 444, 3647
Bhagwan, J., Gupta, A. C., Papadakis, I. E., & Wiita, P. J. 2016, NewA, 44, 21
Bhatta, G., Mohorian, M., & Bilinsky, I. 2018, A&A, 619, A93
Błażejowski, M., Blaylock, G., Bond, I. H., et al. 2005, ApJ, 630, 130
Böttcher, M., & Dermer, C. D. 2010, ApJ, 711, 445
Brinkmann, W., Papadakis, I. E., den Herder, J. W. A., & Haberl, F. 2003, A&A, 402, 929
Brinkmann, W., Papadakis, I. E., Raeth, C., Mimica, P., & Haberl, F. 2005, A&A, 443, 397
Brinkmann, W., Sembay, S., Griffiths, R. G., et al. 2001, A&A, 365, L162
Bulbul, E., Kraft, R., Nulsen, P., et al. 2020, ApJ, 891, 13
Burbidge, G. R., Jones, T. W., & O'Dell, S. L. 1974, ApJ, 193, 43
Chatterjee, R., Das, S., Khasnovis, A., et al. 2021, Short-Timescale Variability of the Blazar Mrk 421 from AstroSat and Simultaneous Multi-Wavelength Observations, arXiv, doi: 10.48550/ARXIV.2102.00919
Dhiman, V., Gupta, A. C., Gaur, H., & Wiita, P. J. 2021, MNRAS, 506, 1198
Donnarumma, I., Vittorini, V., Vercellone, S., et al. 2009, ApJL, 691, L13
Edelson, R. A., & Krolik, J. H. 1988, ApJ, 333, 646
Falomo, R., Kotilainen, J. K., & Treves, A. 2002, ApJL, 569, L35
Ferrero, E., Wagner, S. J., Emmanoulopoulos, D., & Ostorero, L. 2006, A&A, 457, 133
Fossati, G., Buckley, J. H., Bond, I. H., et al. 2008, ApJ, 677, 906
Fossati, G., Celotti, A., Chiaberge, M., et al. 2000a, ApJ, 541, 166
Fossati, G., Celotti, A., Chiaberge, M., et al. 2000b, ApJ, 541, 153
Fossati, G., Celotti, A., Chiaberge, M., et al. 2000c, ApJ, 541, 166
Gaur, H., Gupta, A. C., Lachowicz, P., & Wiita, P. J. 2010, ApJ, 718, 279
Ghiselllini, G., Villata, M., Raiteri, C. M., et al. 1997, A&A, 327, 61
Goyal, A. 2020, MNRAS, 494, 3432
Goyal, A., Gopal-Krishna, Anupama, G. C., et al. 2009, MNRAS, 399, 1622

Gupta, A. 2018, Galax, 6, 1
Gupta, A. C. 2020, Galax, 8, 64
Gupta, A. C., Banerjee, D. P. K., Ashok, N. M., & Joshi, U. C. 2004, A&A, 422, 505
Gupta, A. C., Kalita, N., Gaur, H., & Duorah, K. 2016, MNRAS, 462, 1508
Horan, D., Acciari, V. A., Bradbury, S. M., et al. 2009, ApJ, 695, 596
Isobe, N., Sugimori, K., Kawai, N., et al. 2010, PASJ, 62, L55
Kalita, N., Gupta, A. C., Wiita, P. J., Bhagwan, J., & Duorah, K. 2015, MNRAS, 451, 1356
Kataoka, J., & Stawarz, Ł. 2016, ApJ, 827, 55
Kirk, J. G., Rieger, F. M., & Mastichiadis, A. 1998, A&A, 333, 452
Lachowicz, P., Gupta, A. C., Gaur, H., & Wiita, P. J. 2009, A&A, 506, L17
Lichti, G. G., Bottacini, E., Ajello, M., et al. 2008, A&A, 486, 721
Lin, Y. C., Bertsch, D. L., Chiang, J., et al. 1992, ApJL, 401, L61
Malizia, A., Capalbi, M., Fiore, F., et al. 2000, MNRAS, 312, 123
Maraschi, L., Fossati, G., Tavecchio, F., et al. 1999, ApJL, 526, L81
Markowitz, A., & Edelson, R. 2004, ApJ, 617, 939
Michelson, P. F., Lin, Y. C., Nolan, P. L., et al. 1992, IAU Circ., 5470, 2
Miller, H. R., Carini, M. T., & Goodrich, B. D. 1989, Natur, 337, 627
Mohorian, M., Bhatta, G., Adhikari, T. P., et al. 2021, MNRAS, 510, 5280
Mücke, A., Protheroe, R. J., Engel, R., Rachen, J. P., & Stanev, T. 2003, APh, 18, 593
Padovani, P., & Giommi, P. 1995, ApJ, 444, 567
Pandey, A., Gupta, A. C., & Wiita, P. J. 2017, ApJ, 841, 123
Pandey, A., Gupta, A. C., & Wiita, P. J. 2018, ApJ, 859, 49
Park, T., Kashyap, V. L., Siemiginowska, A., et al. 2006, ApJ, 652, 610
Pavana Gowtami, G. S., Gaur, H., Gupta, A. C., et al. 2022, MNRAS, 511, 3101
Peretz, U., & Behar, E. 2018, MNRAS, 481, 3563
Pian, E., Türler, M., Fiocchi, M., et al. 2014, A&A, 570, A77

Punch, M., Akerlof, C. W., Cawley, M. F., et al. 1992, Natur, 358, 477
Ravasio, M., Tagliaferri, G., Ghisellini, G., & Tavecchio, F. 2004, A&A, 424, 841
Romero, G. E., Cellone, S. A., & Combi, J. A. 1999, A&AS, 135, 477
Sambruna, R. M. 2000, in Proc. of the VSOP Symp., Astrophysical Phenomena Revealed by Space VLBI, ed. H. Hirabayashi, P. G. Edwards, & D. W. Murphy (Sagamihara: Institute of Space and Astronautical Science), 227
Schubnell, M., Akerlof, C. W., Cawley, M. F., et al. 1993, in AIP Conf. Proc. 276, Very High Energy Cosmic-Ray Interactions, ed. L. Jones (Melville, NY: AIP), 185
Sembay, S., Edelson, R., Markowitz, A., Griffiths, R. G., & Turner, M. J. L. 2002, ApJ, 574, 634
Tramacere, A., Giommi, P., Perri, M., Verrecchia, F., & Tosti, G. 2009, A&A, 501, 879
Tramacere, A., Massaro, F., & Cavaliere, A. 2007, A&A, 466, 521
Ulrich, M. H., Kinman, T. D., Lynds, C. R., Rieke, G. H., & Ekers, R. D. 1975, ApJ, 198, 261
Urry, C. M., & Padovani, P. 1995, PASP, 107, 803
Urry, C. M., Treves, A., Maraschi, L., et al. 1997, ApJ, 486, 799
Vaughan, S., Edelson, R., Warwick, R. S., & Uttley, P. 2003, MNRAS, 345, 1271
Wagner, S. J., & Witzel, A. 1995, ARA&A, 33, 163
Wu, X.-B., Liu, F. K., & Zhang, T. Z. 2002, A&A, 389, 742
Yan, D., Yang, S., Zhang, P., et al. 2018, ApJ, 864, 164
Zhang, Y. H., Treves, A., Celotti, A., et al. 2002, ApJ, 572, 762
Zhang, Y. H., Treves, A., Maraschi, L., Bai, J. M., & Liu, F. K. 2006, ApJ, 637, 699
Zhang, Z., Gupta, A. C., Gaur, H., et al. 2019, ApJ, 884, 125
Zhang, Z., Gupta, A. C., Gaur, H., et al. 2021, ApJ, 909, 103